Journal of Materials Chemistry A

PAPER

View Article Online
View Journal | View Issue

Wide electrochemical window ionic salt for use in electropositive metal electrodeposition and solid state Li-ion batteries†

Cite this: J. Mater. Chem. A, 2014, 2, 2194

Sankaran Murugesan,[a] Oliver A. Quintero,[a] Brendan P. Chou,[a] Penghao Xiao,[a] Kyusung Park,[b] Justin W. Hall,[a] Richard A. Jones,[a] Graeme Henkelman,[a] John B. Goodenough[b] and Keith J. Stevenson*[a]

Received 4th December 2013
Accepted 4th December 2013

DOI: 10.1039/c3ta15010k

www.rsc.org/MaterialsA

A stable hydrophobic ionic crystalline solid comprised of the *N*-propyl-*N*-methylpiperidinium cation and hexafluorophosphate anion $PP_{13}PF_6$ exhibits a remarkably wide electrochemical window of 7.2 V. This high purity crystalline ionic salt has versatility for use as an electrolyte in the electrodeposition of reactive metals such as tin. Moreover, this ionic salt can be used as a solid state electrolyte in Li-ion batteries. Theoretical calculations indicate that this solid state electrolyte has vacant sites that are preferential for Li-ion conductivity with an energy barrier of 0.4 eV. Further, the ionic crystals exhibit molecular rotations which facilitate facile Li-ion transport.

1. Introduction

Recently, much research has been dedicated toward developing room-temperature ionic liquids (RTIL) that have readily made a name for themselves as "next-generation" electrolytes.[1–11] They are also of interest as advanced high-temperature lubricants, as well as to treat nuclear waste and replace traditional organic solvents as "green" solvents, reducing environmental levels of volatile organic carbon.[1,10] RTILs are composed of organic cations such as substituted imidazolium ions or tetraalkylammonium ions and of inorganic or organic anions such as $AlCl_4^-$, PF_6^-, BF_4^-, $CF_3SO_3^-$ and $(CF_3SO_2)_2N^-$ ($TFSI^-$). These salts experience weak interactions between their irregularly sized cations and anions, so they exist as liquids below 100 °C.[1] RTILs have inherent ionic conductivity due to presence of excess charge carriers, thereby eliminating the need for using an additional supporting electrolyte in electrochemical devices. RTILs can be used as electrolytes involving electrodeposition of reactive metals (Sn, Si and Ge), metal chalcogenides[12,13] and for Li-ion batteries (LIBs).[4] Moreover, ionic liquids show promise to overcome safety issues related to various electrochemical processes as they are thermally and hydrolytically stable, non-flammable, non-corrosive, and have no measurable vapour pressure up to 200 °C.[1,3–6]

The electrochemical potential window of stability of an ionic liquid is generally characterized by the reduction potential of its cation and the oxidation potential of its anion.

$$\text{Potential window} = E_{\text{anodic limiting potential}} - E_{\text{cathodic limiting potential}} \quad (1)$$

These limits are tunable based on the cation and anion selection, and the electrochemical window can be widened or narrowed to include or exclude certain potential window ranges, an indication of the versatility of ionic liquids in different applications. Often, when ionic liquids are cooled, crystalline solids with orientational disorder are formed; they are known as plastic crystals. Plastic crystals have recently attracted increasing interest owing to their high conductivity and fast ion transport. These crystals exhibit states of coupling with a definite three-dimensional lattice, but some translational motion of a fraction of the species is retained.[5,14–16] This plasticity is highly desirable in electrochemical devices, since it reduces the issue of poor contact between the electrolyte and the electrodes that volume changes can cause while eliminating the leakage problems associated with liquid electrolytes.[5,17] Thus, there is significant interest in the use of plastic crystals in applications such as Li-ion batteries. The mechanically as well as chemically robust nature of these electrolytes is demonstrated by the ability to withstand high applied potentials without any apparent sign of degradation. This ability offers the possibility of very long cycle-life devices and prevention of electrolyte degradation issues associated with the application of high-voltage cathode materials currently under development.[17–19]

[a]*Department of Chemistry, The University of Texas at Austin, 1 University Station, Austin, Texas, 78712, USA. E-mail: stevenson@mail.cm.utexas.edu; Fax: +1-512-471-8696; Tel: +1-512-232-9160*

[b]*Texas Materials Institute and Materials Science and Engineering Program, The University of Texas at Austin, Austin, Texas, 78712, USA*

† Electronic supplementary information (ESI) available: ESI mass spectrum, ^{31}P solution NMR and powder XRD of $PP_{13}PF_6$. XRD analysis of electrodeposited Sn metal over stainless steel electrodes. The electrostatic potentials of Li and $PP_{13}PF_6$. Movie of Li-ion migration and molecular motion. CCDC 960982. For crystallographic data in CIF or other electronic format see DOI: 10.1039/c3ta15010k

The performance of a battery depends on various parameters allowed by the components of the battery. These parameters include: the electrochemical potential of both the anodic and cathodic reactions, the electronic and ionic conductivities of the electrodes used, reversibility of the Li-ion insertion into the electrodes, the potential window of the electrolyte, the ionic conductivity of the electrolyte, and the chemical and electrochemical compatibilities of the electrode and electrolyte.[20,21] The electrochemical potentials for both positive (cathode) and negative (anode) electrodes are important determining factors for what voltage the charging–discharging process of an electrochemical cell requires. Recently, Ceder *et al.*, have shown how the electrochemical potential window of stability for RTILs can be tuned by changing different anion and cation compositions through theoretical calculations.[22] From their calculations it was revealed that the *N*,*N*-propylmethylpyrrolidinium (P_{13}^+) cation can form compounds with different anions, hexafluorophosphate (PF_6), tetrafluoroborate (BF_4), and bis(trifluoromethylsulfonyl)imide (TFSI) with varied electrochemical window. From the analysis PF_6^- anion has shown wide voltage window (5.2 V) compared to other anions. This increased electrochemical window is due to the presence of more electron withdrawing fluorine, F. This effect also studied in the literature with different electrolyte showing that the change in the anion with F shows more hydrophobicity then that of other anions ($[FAP]^- > [NTf_2]^- > [PF_6]^- > [BF_4]^- >$ halides).[23] Concurrently experimental efforts were undertaken to synthesis series of salt based on *N*-methyl-*N*-alkylpyrrolidinium cation and the PF_6^- anion, are reported and their thermal properties described without electrochemical properties.[24] In this context, we have pursued the synthesis of a new ionic liquid based on the *N*-propyl-*N*-methylpiperidinium (PP_{13}^+) cation, instead of pyrrolidinium (P_{13}^+), and the hexafluorophosphate (PF_6^-) anion to prepare the $PP_{13}PF_6$ ionic liquid. An analogous ionic liquid PP_{13}^+ with $TFSI^-$ anion ($PP_{13}TFSI$) has shown a wide electrochemical window (5.9 V) and the electrochemical property of $P_{13}TFSI$ is similar to $PP_{13}TFSI$.[25,26] $PP_{13}TFSI$ has been used in different applications such as LIBs and metal chalcogenide electrodeposition.[12,26] To the best of our knowledge, there are no previous reports describing the synthesis of $PP_{13}PF_6$.

In this work, we report the synthesis and characterization of the ionic liquid $PP_{13}PF_6$ and its physicochemical characterization by mass spectrometry, FTIR, thermal analysis, solution and solid state NMR, single crystal X-ray diffraction, and elemental microanalysis. The synthesized ionic salt is evaluated as an electrolyte for the electrochemical deposition of electropositive metallic tin and as a solid state electrolyte for a rechargeable Li-ion battery. Theoretical calculations support the experimental measurements of an electrochemical window of stability and as a Li-ion conducting solid state electrolyte.

2. Experimental section

2.1. Synthesis of $PP_{13}PF_6$

$PP_{13}PF_6$ was synthesized by the method previously reported for $PP_{13}TFSI$ (*N*-methyl-*N*-propylpiperidinium bis(trifluoromethanesulfon)imide), with minor modifications.[3] The synthesis of $PP_{13}PF_6$ began with preparation of $PP_{13}Br$. In a round bottom flask, 1-bromopropane (45.45 mL, 0.50 mol) and *N*-methylpiperidine (60.66 mL, 0.50 mol) were mixed with 100 mL of acetonitrile and heated (70 °C) while stirring (12 h). The resulting white crystalline precipitate of $PP_{13}Br$ was then washed with acetonitrile and placed in a drying oven overnight. The $PP_{13}Br$ (22.21 g, 0.10 mol) was then mixed with $LiPF_6$ (15.19 g, 0.10 mol) dissolved in 100 mL of ethanol and the resulting mixture stirred at room temperature (24 h). The mixture was extracted with dichloromethane (CH_2Cl_2) and the extracts subjected to column chromatography on a column consisting of Norit activated carbon (5 g) and Fisher neutral alumina (20 g). Removal of solvent resulted in a clear, white solid that was crushed to produce a fine powder, which was placed in a drying oven to remove residual solvent. The product was stored in a desiccator until used. mp: 100 ± 2.5 °C; ^{1}H NMR (500 MHz, CD_2Cl_2): 3.28 (t, J = 7, 4H), 3.21 (m, 2H), 2.99 (s, 3H), 1.87 (br, 4H), 1.72 (m, 4H), 1.01 (t, J = 7, 3H); ^{13}C{H} NMR (126 MHz): 66.1, 61.9, 48.3, 21.2, 20.4, 15.8, 10.8; ^{19}F NMR (470 MHz): −72.6 (d, J = 711); ^{31}P NMR (202 MHz): −143.7 (sep, J = 711); FTIR (diamond ATR): ν_{CH}: 2980 (m), 2955 (m), 2887 (m), 2866 (m), ν_{PF}: 819 (*vs.*), δ_{FPF}: 555 (*vs.*) cm^{-1}; HRMS (ESI) calcd for $C_9H_{20}N^+$: 142.15903, found: 142.15909, calcd for PF_6^-: 144.96473, found: 144.96474; anal. calcd for $C_9H_{20}F_6NP$: C, 37.63%; H, 7.02%; N, 4.88%; found: C, 37.64%; H, 6.93%; N, 4.47%.

2.2. Characterization of $PP_{13}PF_6$

Solution-state ^{1}H, ^{13}C{^{1}H}, ^{19}F, and ^{31}P{^{1}H} NMR spectra were obtained on a Varian INOVA 500 spectrometer in CD_2Cl_2 at room temperature. ^{1}H and ^{13}C chemical shifts were internally referenced to the solvent resonances. ^{19}F and ^{31}P{^{1}H} chemical shifts were externally referenced to $CFCl_3$ in $CDCl_3$ and 85% H_3PO_4, respectively. Solid-state ^{31}P{^{1}H} MAS NMR spectra were obtained on a Bruker Avance 400 spectrometer equipped with a standard 4 mm MAS probe head, using a single-pulse (40°) sequence with a relaxation delay of 5 s and at different spinning rates in the presence of high power ^{1}H decoupling. The ^{31}P chemical shifts were externally referenced to H_3PO_4. All chemical shifts are reported in ppm and coupling constants reported in Hz. FTIR spectra were obtained on a Thermo Scientific Nicolet iS50 spectrometer. Mass spectra were obtained from methanolic solutions on an Agilent 6530 Q-TOF LC/MS spectrometer. Elemental analysis was performed by Galbraith Laboratories. Thermal analysis was performed on a Mettler Toledo TGA/DSC 1 thermogravimetric analyzer from 30 to 500 °C at a heating rate of 5 °C min^{-1}. Melting points were obtained on an Electrothermal Melting Point Apparatus 8000 at a heating rate of 8 °C min^{-1}.

2.3. Electrochemical measurements

Cyclic voltammetry (CV, scan rate 5 mV s^{-1}) was used to evaluate the electrochemical stability window of the ionic liquids. The $PP_{13}PF_6$ was loaded into a three-electrode cell with a glassy

carbon working electrode, graphite counter electrode, and Ag quasi reference electrode (QRE) and heated to 100 °C on a Thermolyne Nuova II stir plate.

2.4. Sn electrodeposition

The $PP_{13}PF_6$ and SnTFSI mixture was evaluated with a cell in a crucible with sand heated to 100 °C on a Thermolyne Nuova II stir plate with a stainless steel working electrode, platinum counter electrode, and Ag (QRE). All CVs were performed with a CH Instruments Electrochemical Workstation CHI 440.

2.5. Li-cell construction

Solid state Teflon cells were used for impedance testing. Prior to adding the electrolyte, the cell was washed with acetone and Teflon tape was wrapped around the joints. After purging for 15 minutes with argon gas in an MBraun glovebox, 300 mg $PP_{13}PF_6$ and 30 mg LiTFSI were vigorously pounded and mixed together. The asymmetric cell also included a Li electrode cut from a Li sheet. The electrolyte was then added into the cell and the cell was sealed. The current collector was a stainless steel rod. After removing from the glove box, the cell was wrapped in Teflon tape.

2.6. Impedance testing of Li cell

Impedance testing of the solid state cell was conducted with a Solartron FRA/Impedance Analyzer. Impedance analysis was conducted at 5 °C intervals from room temperature to 45 °C. At each temperature, the conditions were left to equilibrate for 30 minutes prior to impedance testing. Impedance analysis was conducted from 10^6 Hz to 1 Hz.

2.7. Theoretical methods

All the calculations were performed with the Vienna *ab initio* simulation package with density functional theory (DFT) at the general gradient approximation (GGA) level of theory.[27,28] Valence-electron wave functions were expanded on a plane wave basis set with an energy cutoff of 520 eV; core electrons were incorporated into pseudo-potentials within the projector augmented wave framework.[29,30] For structure optimizations, the Perdue–Wang (PW91) form was chosen for the exchange–correlation energy.[31] For the density of state (DOS) calculations, the Heyd–Scuseria–Ernzerhof (HSE06) hybrid functional was used for $PP_{13}PF_6$ to calculate the band gap and work function.[32]

2.8. Single crystal X-ray crystallography

Single crystals of $PP_{13}PF_6$ were grown by slow evaporation from dichloromethane at ambient temperature. Diffraction data were collected at 163 K on a Rigaku SCX-MINI diffractometer equipped with a Mercury 2 CCD detector using Mo-Kα radiation. Reflections were collected from ω-scans and a multiscan absorption correction was applied with ABSCOR. Structures were solved by direct methods with SHELXS-97 and refined against F^2 by full-matrix least squares methods. All non-hydrogen atoms were refined anisotropically. Hydrogens were located from difference Fourier maps and refined isotropically. Positional disorder of one PF_6 anion was modeled by three equivalent sets of F atoms. The site occupancies of the disorder components were refined with restraint of the sum to unity.

3. Results and discussion

An equimolar quantity of $PP_{13}Br$ and $LiPF_6$ were reacted in ethanol and further extraction with CH_2Cl_2 resulted in fine white powder upon solvent removal. This white crystalline powder was recrystallized twice from CH_2Cl_2. The recrystallized powder was characterized with different spectroscopic and thermal probes. Initially, the melting point of the compound was tested in a capillary tube melting point experiment and it was found to be 100 ± 2.5 °C.

3.1. Characterization of solid ionic liquid crystals

The observed melting point is significantly different from those of the reactants $PP_{13}Br$ (250 °C) and $LiPF_6$ (310 °C) used in the reaction, which is consistent with formation of the product. This melting point was further confirmed by TGA-DSC analysis, which showed a phase change at 100 °C and complete decomposition around 400 °C in a N_2 atmosphere (Fig. 1A).

The white, crystalline solid was further characterized by mass spectrometry and NMR to confirm its chemical structure.

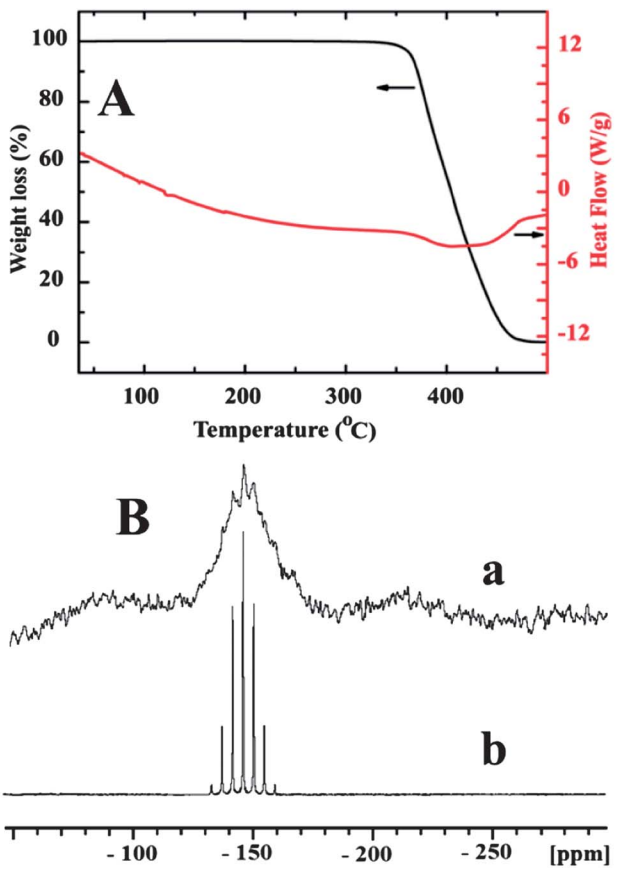

Fig. 1 (A) Thermogravimetric analysis of $PP_{13}PF_6$ in N_2 atmosphere. (B) ^{31}P MAS NMR spectra recorded at a spinning rate of 6 kHz for $LiPF_6$ (a) and $PP_{13}PF_6$ (b).

First, electrospray ionization mass spectrometry (ESI-MS) was used to confirm the presence of the molecular ions in the compound. Both the PP_{13} and PF_6 ions were observed, at 142.159 *m*/*z* and 144.964 *m*/*z*, in positive and negative ion modes respectively (ESI, Fig. S1f and S1g†). Solution state ^{19}F and $^{31}P\{^1H\}$ NMR spectra (ESI, Fig. S1c and S1d†) were consistent with the presence of the PF_6^- anion ($\delta_P = -143.7$ ppm, $\delta_F = -72.6$ ppm, $^1J_{PF} = 711$ Hz).[11,33,34] Similarly, the ^1H and $^{13}C\{^1H\}$ spectra were consistent with the PP_{13}^+ cation (ESI, Fig. S1a and S1b†). To further investigate the PF_6^- environment in crystalline $PP_{13}PF_6$ at room temperature, a solid state CP MAS ^{31}P NMR spectrum was obtained. The spectrum of $PP_{13}PF_6$ contained a well resolved septuplet at −146.3 ppm ($^1J_{PF} = 713$ Hz), with a line width of 47 Hz and very low sidebands (Fig. 1B). By comparison, $LiPF_6$ showed a very broad isotropic resonance at −146.3 ppm accompanied by intense sidebands. The decreased line width in $PP_{13}PF_6$ can be attributed to faster PF_6^- motions in $PP_{13}PF_6$ *versus* $LiPF_6$. This evidence further demonstrates the significant molecular motion of the PF_6^- ion in $PP_{13}PF_6$ at room temperature. Recently, Jin *et al.*[14] observed the change in PF_6^- orientation in the plastic crystal $[P_{1,2,2,4}][PF_6]$ through temperature dependent ^{31}P NMR analysis. $PP_{13}PF_6$ was further characterized with a FTIR spectrum (Fig. S1e†), which confirms the presence of alkyl groups, due to aliphatic C–H stretches at 2980, 2955, 2887, and 2866 cm^{-1}. The spectrum also confirms the presence of the PF_6^- anion, due to the intense P–F stretching and F–P–F bending modes at 819 and 755 cm^{-1} respectively.[35]

3.2. Solid state structure

$PP_{13}PF_6$ crystallizes in the $P2_1/c$ space group with two crystallographically distinct ion pairs in the asymmetric unit, packing in alternating layers of PP_{13} and PF_6 ions along the *a*-axis, as shown in Fig. 2. This layering provides a relatively unobstructed diffusion path for Li-ions between PF_6^- anions. In contrast to the previously reported salt $PP_{13}Al(hfip)_4$, the *N*,*N*-methypropylpyridinium cation in $PP_{13}PF_6$ is not positionally disordered in the solid state.[49] This observation is consistent with the higher observed melting point of 100 °C *vs.* 69 °C. The ordering of the cation is stabilized by many close interactions (average distance 2.54 Å) between the hydrogens of the cation and the fluorines of the anion, slightly shorter than the sum of their van der Waals radii (2.67 Å). However, the interactions are still considered only weak hydrogen bonds according to the generally accepted definition (>2.2 Å).[50] Accordingly, there is still orientational disorder of the PF_6^- anion observed at 163 K, with one of the anions disordered over three sites.

3.3. Electrochemical potential window of stability for $PP_{13}PF_6$

Cyclic voltammetry was performed to determine the electrochemical potential window of stability of the ionic salt. The experiments were performed at 100 °C with a Ag (QRE) and graphite counter electrode. Fig. 3A shows the cyclic voltammogram of $PP_{13}PF_6$ having an anodic limiting potential (E_{AL}) of 4.3 V and cathodic limiting potential (E_{CL}) of −3.25 V, which is similar to decomposition of PP_{13}^+ in $PP_{13}TFSI$.[25] The

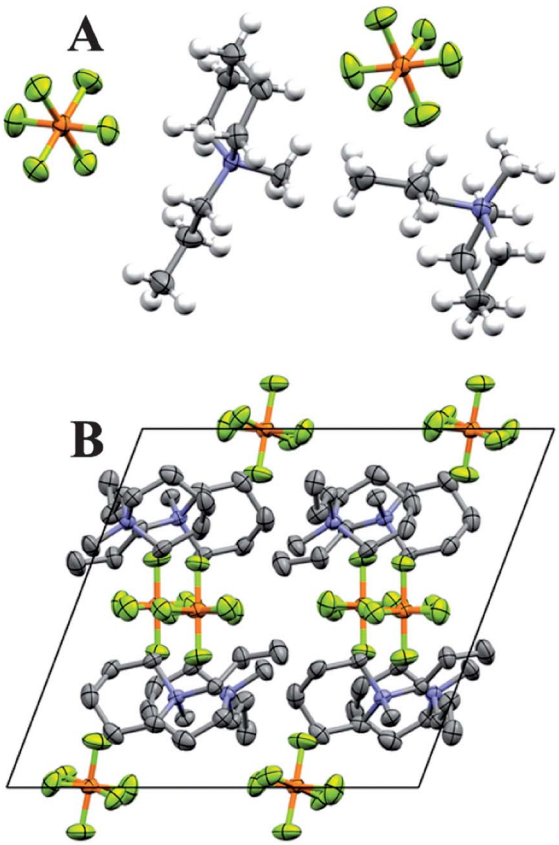

Fig. 2 X-ray crystal structure of $PP_{13}PF_6$ at 223 K (50% thermal ellipsoids): (A) asymmetric unit (hydrogens as fixed spheres of radius 0.30 Å) (B) unit cell viewed along the *b*-axis (hydrogens omitted for clarity).

electrochemical potential window of the $PP_{13}TFSI$ was measured as a comparison to the newly synthesised $PP_{13}PF_6$ ionic solid. The $PP_{13}TFSI$ ionic liquid was synthesized by adopting an earlier reported procedure and the electrochemical window determined as previously reported.[2] The current fluctuations above −3.5 V and weak anodic current around 1 V *vs.* Ag (QRE) may be due to the unstable decomposition of the ionic liquid and the presence of impurities.[25] The $PP_{13}TFSI$ cathodic limiting potential E_{CL} at −3.25 V and anodic limiting potential E_{AL} at 2.68 V *vs.* Ag (QRE) result in a 5.9 V potential window.[25] The $PP_{13}PF_6$, showed a remarkably wide electrochemical window of 7.2 V with E_{CL} at −3.25 V and E_{AL} at 3.95 V. This increased electrochemical window is due the presence of more electron withdrawing fluorine which also increases the hydrophobicity. This result suggests not only that the ionic solid had negligible impurities (being crystalline), but also that it could serve as a promising electrolyte for the electrodeposition of several kinds of reactive (electropositive) metals.

The experimentally determined potential window was verified by DFT calculations. The work functions are calculated to align the Fermi-level of Li and the electrolyte (Fig. 3B). The work function of Li and $PP_{13}PF_6$ are calculated as 3.00 and 8.58 eV, respectively, resulting in a Fermi-level of Li of 5.58 eV above $PP_{13}PF_6$. The band gap of $PP_{13}PF_6$ is calculated as 7.98 eV. Both the band-gap and work-function calculations were performed

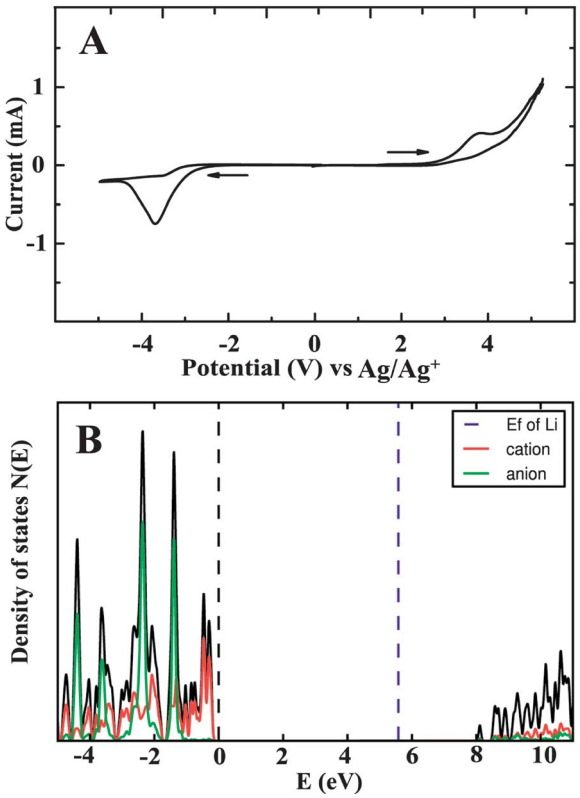

Fig. 3 (A) Cyclic voltammograms of $PP_{13}PF_6$ at 100 °C. Third cycle is shown. (B) Calculated density of states of $PP_{13}PF_6$.

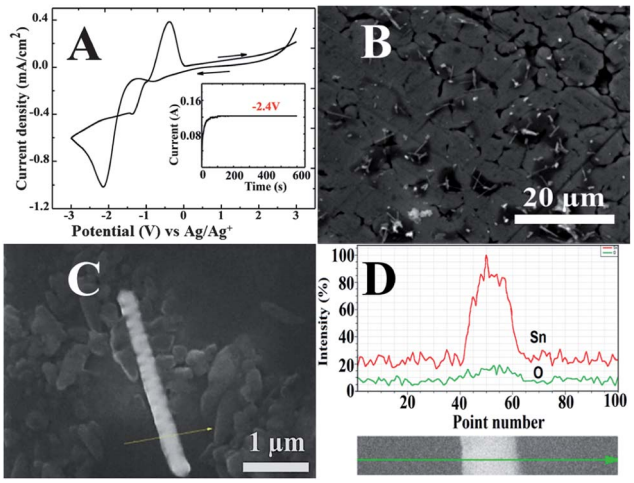

Fig. 4 (A) Cyclic voltammogram of Sn electrodeposition over stainless steel electrodes at the scan rate of 10 mV s^{-1} with SnTFSI mixed with $PP_{13}PF_6$ heated at 100 °C using graphite rod as counter and Ag (QRE). Third cycle is shown. Inset figure shows the i–t curve ($T = 100$ °C, V = −2.4 V, working electrode: stainless steel) and (B). SEM image of the electrodeposited Sn over stainless steel electrodes (C & D). EDS line scan analysis over Sn nanorod showing the elements present are Sn and minimal oxygen contamination over the surface.

with the HSE06 hybrid functional as they are underestimated with pure GGA functionals. The HOMO states are primarily from the cation, PP_{13}, shown as red lines in Fig. 3B. It is therefore possible to further increase the electrochemical window by replacing PP_{13} with other cations with lower HOMO (or higher work function). The powder XRD pattern of $PP_{13}PF_6$ matched well with the theoretically generated XRD pattern from the single crystal structure (Fig. S3†), confirming the composition of the bulk material to be the same as that of the single crystal.

3.4. Electrochemical application of $PP_{13}PF_6$

Electrodeposition of Sn metal. Sn metal is used in various technologies. Specifically, electrodeposited Sn is often used in vacuum microelectronics as a cathode in field-emitters and as an anode in Li-ion batteries.[36,37] Usually, Sn electrodeposition is performed with additives to lower the reduction potential.[38] For example, commercial Sn electroplating has been performed either in highly acidic or alkaline baths with Sn–metal salts.[39,40] The problems with this process includes high cost, toxic experimental setups and investments in waste-treatment methods. These aspects warrant an alternative green-deposition process. We have developed a method for the electrodeposition of Sn without any additives to check the viability of $PP_{13}PF_6$ as an electrolyte. Fig. 4A shows the cyclic voltammogram of the reduction of Sn^{2+} in $PP_{13}PF_6$ at 100 °C at a stainless steel electrode. The electrodeposition of Sn can be performed on different conductors such as glassy carbon and stainless steel. Chronoamperometric deposition was performed at −2.4 V *vs.* Ag (QRE) for 600 s (inset Fig. 4A); it showed a steep rise in current for about 100 s and then saturation indicated the completion of the deposition process. The electrodeposited Sn over stainless steel electrodes was characterized by SEM-EDS analysis. Fig. 4B shows the rod shaped morphology of the chronoamperometrically deposited Sn. The rod morphology of Sn was further characterized by elemental analysis through an EDS line scan across the rod (Fig. 4C). The elements present in the rod were mainly Sn, and the oxygen level was a negligible amount (Fig. 4D). XRD of electrodeposited Sn matched well with the JCPDS # 65-2631 for pure Sn metal (Fig. S2†). These results clearly show that the electrodeposited materials are pure Sn with rod shaped morphology. The rod morphology is of great interest for field-emitter transistor applications.[36,41]

3.5. Li-ion transport in a solid state LIB

Solid electrolytes for Li-ion transport are receiving considerable interest owing to rising concerns with liquid electrolytes, *e.g.* solvent leakage, flammability and safety hazards. The development of a Li-ion solid electrolyte with high low-temperature conductivity and a wide electrochemical window is necessarily of high priority. Recently, sulfide based glasses have shown good Li-ion conductivity of about 12 mS cm^{-1} at room temperature;[42] however, the synthesis of these materials requires stringent procedures, a long time, and high temperatures, which means a high-energy process.[43,44] Furthermore, it is important to understand the interfacial Li-ion transfer resistance across the electrode/electrolyte interface in an all-solid-state cell.

Understanding ion transport through the plastic crystals for application in solid state devices is very important.[14] It was hypothesized that the conduction in these kinds of plastic crystals is enhanced by the rotator motions of the anions supporting the motion of Li-ion from one cation site to another.[5] It has been shown that when these plastic crystals are doped with Li-ion, they exhibit fast Li-ion conduction for use in rechargeable batteries.[45] Applications of the plastic crystals as an electrolyte for rechargeable all-solid-state Li batteries are promising. Crystalline ceramics and glassy thin films could be used as the electrolyte, but they are generally brittle, which makes it difficult to form large-area membranes, and they have a high interfacial contact resistance with solid electrolyte. On the other hand, use of a polymer-based electrolyte system such as the polyethylene oxide (PEO) membrane showed that the Li-ion movement by the dynamics of the polymer chains and the overall ionic conductivity of the system is low. In this context, the Li-ion doped plastic crystals showed enhanced Li-ion conductivity as high as 2×10^{-4} S cm^{-1} at 60 °C.[45] We wanted to test the Li-ion conductivity of newly synthesized $PP_{13}PF_6$ ionic crystals. We mixed these crystals with 10 wt% of LiTFSI salt as the Li-ion source. To evaluate the conductivity, symmetric (Stainless Steel block/$PP_{13}PF_6$ + 10 wt% LiTFSI)/(Stainless Steel block) and asymmetric Swagelok Teflon cells (Li metal/$PP_{13}PF_6$ + 10 wt% LiTFSI)/(Stainless Steel block) cells were constructed. The conductivity of the symmetric and asymmetric cells showed enhanced Li-ion transport with increasing temperature (Fig. 5). The conductivity of the asymmetric system was in the order of 2.4×10^{-4} S cm^{-1} at 45 °C, which is higher than that of Li-ion conductivity reported previously for Li-ion doped plastic crystals measured at 60 °C.[45] The conductivity at different temperatures for symmetric and asymmetric configurations is given in the ESI, Table S1.† The difference in the conductivity of the symmetric and asymmetric cells was about 50 kJ due to the difference in activation energy for Li-ion transfer across the anode/electrolyte interface. In these measurements, there was no polymer membrane used to prevent contact between the Li metal anode and the stainless steel blocks, which suggests that these electrolytes are attractive for application in Li metal batteries.

The stability of the electrolyte was tested by cyclic voltammetry of the asymmetric cell (Li metal/$PP_{13}PF_6$ + 10 wt% LiTFSI)/(Stainless Steel block) at different temperatures (Fig. S6†). The measurements were performed at 30 °C, 35 °C, 40 °C and 45 °C between a potential window of −0.5 and 5 V *vs.* Li/Li$^+$ at a scan rate of 2 mV s^{-1}. With an increase in temperature, the ionic conductivity of the system increased and displayed a wide potential window of stability. This stable window is due to the strong hydrogen bonded PF_6^- anions; the motion of these anions facilitates the Li-ion conductivity and stability. The electrochemical window of stability is wider than that of polymer based electrolytes (3.8 V *vs.* Li/Li$^+$).[46]

3.6. Theoretical calculation of Li-ion diffusion mechanism

To understand the enhanced Li-ion transport in the $PP_{13}PF_6$ ionic crystals, DFT calculations were performed to find the Li-ion diffusion barrier in the crystals. The minimum energy path of Li-ion diffusion as calculated with the nudged elastic band method is shown in Fig. 6.[47,48] The inset atomic structures show that Li-ion is coordinated by three F atoms from two PF_6 groups for each minimum along the path. In the diffusion process, Li-ion moves in concert with PF_6 octahedral rotation, to maintain a high coordination. The process is analogous to people (representing Li-ion) walking through a revolving door (PF_6 groups). At the saddle point, only one Li–F bond is broken. A movie of this concerted molecular rotation and Li-ion diffusion is provided in the ESI.† The energy barrier for PF_6 rotation where no Li–F bond is broken is very small. The rotation can be

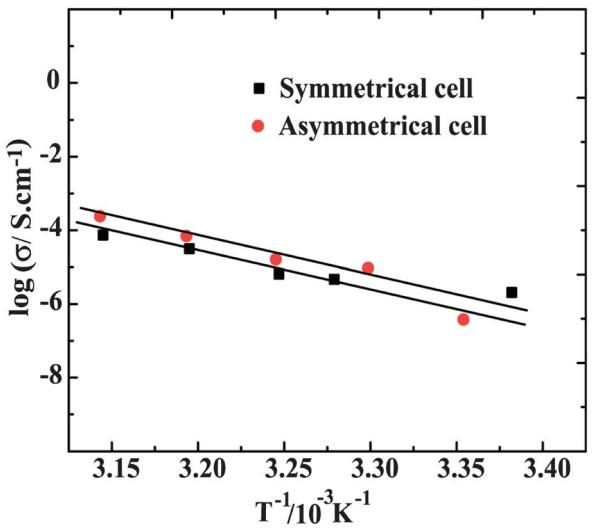

Fig. 5 Arrhenius plot of Li-ion conductivity in the symmetric and asymmetric cells of the $PP_{13}PF_6$ ionic crystal.

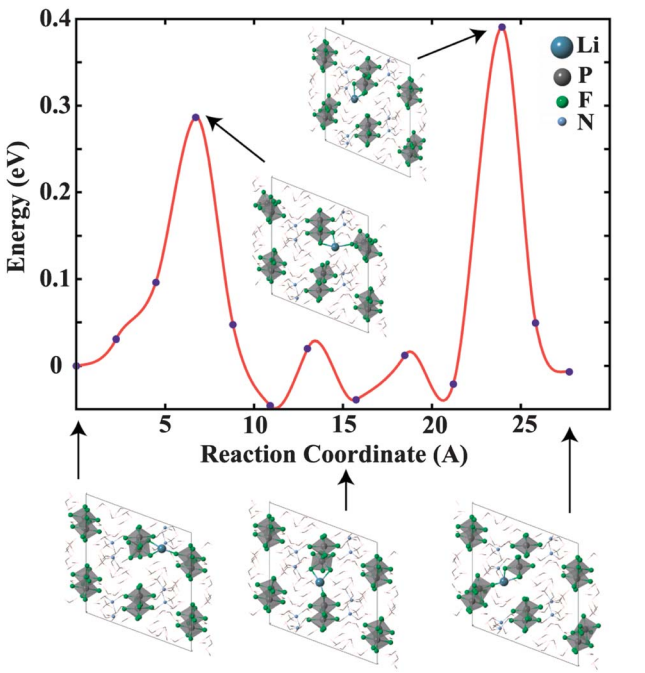

Fig. 6 The minimum energy path for Li-ion diffusion in $PP_{13}PF_6$.

observed in *ab initio* molecular dynamic simulations (MD) at room temperature in the time scale of a picosecond (see ESI†).

The maximum energy barrier for the Li-ion to migrate in the crystals is 0.4 eV, which is lower than in other solid state electrolytes used in Li metal batteries.[49–51] These calculations are consistent with the experimental activation energy of 55 kJ mol^{-1} measured in the unsymmetrical (Li metal/$PP_{13}PF_6$ + 10 wt% LiTFSI)/(Stainless Steel block) cell geometry.

4. Conclusions

A high-purity ionic crystal of $PP_{13}PF_6$ stable to water and air has been successfully synthesized and characterized. XRD analysis of the crystal structure confirms that the formation of a solid crystal at room temperature is due to the strong interaction between the F of the PF_6 anion and the H in the PP_{13} cation. This ionic crystal showed a wide electrochemical potential window of stability of 7.2 V. Electrodeposition of electropositive Sn metal results in a rod shaped morphology that may be of interest in microelectronic applications. Ionic crystals showed enhanced Li-ion transport with an ionic conductivity of 2.4×10^{-4} S cm^{-1} at 45 °C. The calculated energy barrier for the Li-ion conductivity of only 0.4 eV matches well with the experimentally determined activation energy. Further, MD simulations indicate that the ionic crystal exhibits facile molecular motions which facilitate Li-ion transport.

Acknowledgements

This work was supported as part of the program "Understanding Charge Separation and Transfer at Interfaces in Energy Materials (EFRC: CST)", an Energy Frontier Research Center funded by the U.S. Department of Energy Office of Science, Office of Basic Energy Sciences, under Award no. DE-SC0001091. Authors Q.A.O and C.P.B thank The Welch Foundation and The University of Texas at Austin for support *via* the Welch Summer Scholar Program. S.M. thanks Vladimir I. Bakhmutov for solid state NMR analysis. R.A.J. thanks The Welch Foundation (F-816) and ACS-PRF (52682-ND10) for financial support.

References

1 M. Armand, F. Endres, D. R. MacFarlane, H. Ohno and B. Scrosati, *Nat. Mater.*, 2009, **8**, 621–629.
2 A. P. Abbott, I. Dalrymple, F. Endres and D. R. Macfarlane, in *Electrodeposition from Ionic Liquids*, Wiley-VCH Verlag GmbH & Co. KGaA, 2008, pp. 1–13.
3 H. Ohno, M. Yoshizawa and T. Mizumo, in *Electrochemical Aspects of Ionic Liquids*, John Wiley & Sons, Inc., 2005, pp. 75–81.
4 A. P. Abbott and K. J. McKenzie, *Phys. Chem. Chem. Phys.*, 2006, **8**, 4265–4279.
5 D. R. MacFarlane and M. Forsyth, *Adv. Mater.*, 2001, **13**, 957–966.
6 T. Belhocine, S. A. Forsyth, H. Q. N. Gunaratne, M. Nieuwenhuyzen, A. V. Puga, K. R. Seddon, G. Srinivasan and K. Whiston, *Green Chem.*, 2011, **13**, 59–63.
7 G. B. Appetecchi, S. Scaccia, C. Tizzani, F. Alessandrini and S. Passerini, *J. Electrochem. Soc.*, 2006, **153**, A1685–A1691.
8 H. Matsumoto, H. Sakaebe, K. Tatsumi, M. Kikuta, E. Ishiko and M. Kono, *J. Power Sources*, 2006, **160**, 1308–1313.
9 G. A. Snook, A. S. Best, A. G. Pandolfo and A. F. Hollenkamp, *Electrochem. Commun.*, 2006, **8**, 1405–1411.
10 H. Sakaebe and H. Matsumoto, *Electrochem. Commun.*, 2003, **5**, 594–598.
11 H.-H. Lee, Y.-Y. Wang, C.-C. Wan, M.-H. Yang, H.-C. Wu and D.-T. Shieh, *J. Appl. Electrochem.*, 2005, **35**, 615–623.
12 S. Murugesan, P. Kearns and K. J. Stevenson, *Langmuir*, 2012, **28**, 5513–5517.
13 S. Murugesan, A. Akkineni, B. P. Chou, M. S. Glaz, D. A. Vanden Bout and K. J. Stevenson, *ACS Nano*, 2013, **7**, 8199–8205.
14 L. Jin, K. M. Nairn, C. M. Forsyth, A. J. Seeber, D. R. MacFarlane, P. C. Howlett, M. Forsyth and J. M. Pringle, *J. Am. Chem. Soc.*, 2012, **134**, 9688–9697.
15 J. M. Pringle, P. C. Howlett, D. R. MacFarlane and M. Forsyth, *J. Mater. Chem.*, 2010, **20**, 2056–2062.
16 J. M. Pringle, *Phys. Chem. Chem. Phys.*, 2013, **15**, 1339–1351.
17 J. Sunarso, Y. Shekibi, J. Efthimiadis, L. Jin, J. Pringle, A. Hollenkamp, D. MacFarlane, M. Forsyth and P. Howlett, *J. Solid State Electrochem.*, 2012, **16**, 1841–1848.
18 P. M. Bayley, A. S. Best, D. R. MacFarlane and M. Forsyth, *Phys. Chem. Chem. Phys.*, 2011, **13**, 4632–4640.
19 U. L. Bernard, E. I. Izgorodina and D. R. MacFarlane, *J. Phys. Chem. C*, 2010, **114**, 20472–20478.
20 J. B. Goodenough, *Acc. Chem. Res.*, 2013, **46**, 1053–1061.
21 J. B. Goodenough and Y. Kim, *Chem. Mater.*, 2009, **22**, 587–603.
22 G. Ceder, S. P. Ong, O. Andreussi, Y. B. Wu and N. Marzari, *Chem. Mater.*, 2011, **23**, 2979–2986.
23 A. M. O'Mahony, D. S. Silvester, L. Aldous, C. Hardacre and R. G. Compton, *J. Chem. Eng. Data*, 2008, **53**, 2884–2891.
24 J. Golding, N. Hamid, D. R. MacFarlane, M. Forsyth, C. Forsyth, C. Collins and J. Huang, *Chem. Mater.*, 2001, **13**, 558–564.
25 H. Ye, J. Huang, J. J. Xu, A. Khalfan and S. G. Greenbaum, *J. Electrochem. Soc.*, 2007, **154**, A1048–A1057.
26 H. Sakaebe and H. Matsumoto, *Electrochem. Commun.*, 2003, **5**, 594–598.
27 W. Kohn and L. J. Sham, *Phys. Rev.*, 1965, **140**, A1133–A1138.
28 W. Kohn, A. D. Becke and R. G. Parr, *J. Phys. Chem.*, 1996, **100**, 12974–12980.
29 P. E. Blöchl, *Phys. Rev. B: Condens. Matter Mater. Phys.*, 1994, **50**, 17953–17979.
30 G. Kresse and D. Joubert, *Phys. Rev. B: Condens. Matter Mater. Phys.*, 1999, **59**, 1758–1775.
31 J. P. Perdew and Y. Wang, *Phys. Rev. B: Condens. Matter Mater. Phys.*, 1992, **45**, 13244–13249.
32 J. Heyd, G. E. Scuseria and M. Ernzerhof, *J. Chem. Phys.*, 2003, **118**, 8207–8215.

33 A. V. Plakhotnyk, L. Ernst and R. Schmutzler, *J. Fluorine Chem.*, 2005, **126**, 27–31.
34 M. Forsyth and M. E. Smith, *Synth. Met.*, 1993, **55**, 714–719.
35 H. Yang, G. V. Zhuang and P. N. Ross Jr, *J. Power Sources*, 2006, **161**, 573–579.
36 C. L. Rinne, J. J. Hren and P. S. Fedkiw, *J. Electrochem. Soc.*, 2002, **149**, C150–C158.
37 C. D. Gu, Y. J. Mai, J. P. Zhou, Y. H. You and J. P. Tu, *J. Power Sources*, 2012, **214**, 200–207.
38 S. Meibuhr, E. Yeager, A. Kozawa and F. Hovorka, *J. Electrochem. Soc.*, 1963, **110**, 190–202.
39 L. E. Stout and A. H. Baum, *Trans. Electrochem. Soc.*, 1937, **72**, 429–446.
40 N. Pewnim and S. Roy, *Electrochim. Acta*, 2013, **90**, 498–506.
41 A. Muller, S. E. C. Dale, M. A. Engbarth, S. J. Bending and L. M. Peter, *CrystEngComm*, 2010, **12**, 2135–2138.
42 N. Kamaya, K. Homma, Y. Yamakawa, M. Hirayama, R. Kanno, M. Yonemura, T. Kamiyama, Y. Kato, S. Hama, K. Kawamoto and A. Mitsui, *Nat. Mater.*, 2011, **10**, 682–686.
43 A. Hayashi, S. Hama, H. Morimoto, M. Tatsumisago and T. Minami, *J. Am. Ceram. Soc.*, 2001, **84**, 477–479.
44 T. Minami and N. Machida, *Mater. Sci. Eng., B*, 1992, **13**, 203–208.
45 D. R. MacFarlane, J. Huang and M. Forsyth, *Nature*, 1999, **402**, 792–794.
46 L. J. A. Siqueira and M. C. C. Ribeiro, *J. Chem. Phys.*, 2005, **122**, 194911.
47 G. Henkelman and H. Jonsson, *J. Chem. Phys.*, 2000, **113**, 9978–9985.
48 G. Henkelman, B. P. Uberuaga and H. Jonsson, *J. Chem. Phys.*, 2000, **113**, 9901–9904.
49 Z. Liu, W. Fu, E. A. Payzant, X. Yu, Z. Wu, N. J. Dudney, J. Kiggans, K. Hong, A. J. Rondinone and C. Liang, *J. Am. Chem. Soc.*, 2013, **135**, 975–978.
50 F. Croce, G. B. Appetecchi, L. Persi and B. Scrosati, *Nature*, 1998, **394**, 456–458.
51 F. Mizuno, A. Hayashi, K. Tadanaga and M. Tatsumisago, *Adv. Mater.*, 2005, **17**, 918–921.